UC Santa Barbara

UC Santa Barbara Previously Published Works

Title

Dynamics of mussel plaque detachment

Permalink

https://escholarship.org/uc/item/2kh7r2tc

Journal

Soft Matter, 11(34)

ISSN

1744-683X

Authors

Desmond, Kenneth W
Zacchia, Nicholas A
Waite, J Herbert
et al.

Publication Date

2015-09-14

DOI

10.1039/c5sm01072a

Peer reviewed

eScholarship.org Powered by the California Digital Library
University of California

Soft Matter

PAPER

Cite this: *Soft Matter*, 2015, **11**, 6832

Dynamics of mussel plaque detachment†

Kenneth W. Desmond,[ab] Nicholas A. Zacchia,[ab] J. Herbert Waite[ac] and Megan T. Valentine*[ab]

Received 5th May 2015,
Accepted 19th July 2015

DOI: 10.1039/c5sm01072a

www.rsc.org/softmatter

Mussels are well known for their ability to generate and maintain strong, long-lasting adhesive bonds under hostile conditions. Many prior studies attribute their adhesive strength to the strong chemical interactions between the holdfast and substrate. While chemical interactions are certainly important, adhesive performance is also determined by contact geometry, and understanding the coupling between chemical interactions and the plaque shape and mechanical properties is essential in deploying bioinspired strategies when engineering improved adhesives. To investigate how the shape and mechanical properties of the mussel's plaque contribute to its adhesive performance, we use a custom built load frame capable of fully characterizing the dynamics of the detachment. With this, we can pull on samples along any orientation, while at the same time measuring the resulting force and imaging the bulk deformations of the plaque as well as the holdfast-substrate interface where debonding occurs. We find that the force-induced yielding of the mussel plaque improves the bond strength by two orders of magnitude and that the holdfast shape improves bond strength by an additional order of magnitude as compared to other simple geometries. These results demonstrate that optimizing the contact geometry can play as important a role on adhesive performance as optimizing the chemical interactions as observed in other organisms and model systems.

1 Introduction

Nature has solved many adhesive problems that confound human engineers. Mussels, barnacles, and even vines generate and maintain strong long-lasting bonds to surfaces in hostile, wet environments, and unlike man-made adhesives, no pretreatment or drying of the surface is required. Recapitulating these abilities in man-made systems would lead to improved adhesives for biomedical, naval, aerospace, and soft robotic applications, and would provide deeper insight into the fundamental mechanisms that control adhesive strength and performance. One successful route for optimizing adhesive performance is the use of bioinspired chemistry, particularly the catechol functionality exploited by many marine lifeforms.[1] However, adhesive performance depends not only on the molecular-level chemistry of the interface, but also on the geometry and mechanics of the holdfast, the load-bearing structure composed of the plaque and thread.

The *Mytilus californianus* mussel provides an excellent model system to examine the role of holdfast shape and mechanics in adhesion. These mussels live in the hostile intertidal zone. Their survival relies on the ability to maintain long-lasting attachments to rocks and piers near the shore while being subjected to a non-stop onslaught of waves that can exert hydrodynamic forces on each mussel in excess of 10 N, as well as the forces exerted by predators hoping to dislodge them for a meal.[2,3] This has led to a strong evolutionary pressure to maximize adhesive performance, with ~10% of the mussels' metabolic energy output devoted to creating and maintaining adhesive bonds.[1]

Mussels achieve strong attachment with a holdfast known as a byssus that contains 25–100 threads distributed radially onto the substrate.[4–6] Each thread (~100 μm in diameter and ~5 cm in length) extends outward from the mussel and terminates at an adhesive plaque that is ~1 mm in diameter (see Fig. 1).[7,8] The thread typically meets the plaque somewhere near the center of the plaque's cross-section at a natural angle of ~5°–45°, depending on how far from the body the plaque was deposited. This contact geometry, which is common among biological systems that require strong, long-lasting bonding, gives the appearance of a mushroom shape.[9–12]

There have been several prior reports of the physical mechanisms of mussel detachment.[8,13,14] These focused primarily on the average force required to detach a holdfast of a given size and shape, and provided important insight into the ability of

[a] *Materials Research Laboratory, University of California Santa Barbara, USA. E-mail: valentine@engineering.ucsb.edu*
[b] *Department of Mechanical Engineering, University of California Santa Barbara, USA*
[c] *Molecular Cell and Developmental Biology Department, University of California Santa Barbara, USA*

† Electronic supplementary information (ESI) available. See DOI: 10.1039/c5sm01072a

This journal is © The Royal Society of Chemistry 2015

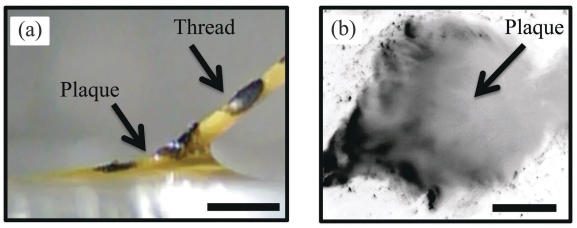

Fig. 1 (a) Side view image of a thread–plaque holdfast, attached to a glass slide. The thread is under tension, and the black marks are painted onto the outer cuticle surface to serve as fiducial markers to enable measurement of sample strain. (b) Image of the plaque–glass interface taken from below to allow for direct observation of detachment dynamics. Scale bars are 1 mm.

mussels to bear loads. However, holdfast detachment is a dynamic process, and a complete understanding of adhesive performance requires not only knowing the detachment force, but also how the holdfast deforms prior to detachment, where failure initiates, and how all these properties depend on loading conditions, including the pull direction and pull rate.[1]

In this study, we investigate the role of holdfast shape and mechanics in the dynamics of detachment using natural mussel-derived holdfasts attached to glass. We find that the shape and mechanical properties of the holdfast provide a 100–1000 fold enhancement in bond strength over that provided by the chemical bonding alone. Moreover, we determine how the adhesive plaques deform prior to detachment and where failure initiates under various loading conditions. These studies reveal the design principles that control the adhesive performance of the natural mussel holdfast, and suggest new approaches to the design of synthetic adhesives.

2 Materials and methods

2.1 Preparation of thread–plaque samples

Mytilus californianus mussels were collected from Goleta Pier (Goleta, CA, USA) and stored in a tank at 12–15 °C in flowing seawater from an offshore intake line in the Pacific Ocean. To enable the deposition of thread–plaque holdfasts onto glass substrates for our study, we immobilized the mussels on top of a single layer of 15 (arranged 3 × 5) microscope slides (each 75 mm × 25 mm) that were tightly packed on top of a large plexiglass plate. Both the slides and mussels were immobilized to the plates using rubber bands. The mussel-attached plates were then placed and maintained in the tank for 1–4 days. The threads that connected the plaques to the mussel were then cut, as close to the mussel body as possible, and the mussels returned to the tank to be used again in future studies. A fraction of the deposited plaques were placed too close to the slide edge or on top of another plaque and were not useful. On average, each mussel produced ~3 useful plaques per day. Each glass slide with useful thread–plaques was rinsed with Milli-Q deionized water and stored for 1–7 days in Milli-Q deionized water at 4 °C before a mechanical measurement was performed. We found no correlation between the detachment force or mode and storage time under these conditions. In total, 110 different plaques from 4 different mussels over a 2 month period were tested in this study.

2.2 Tensile testing experiment

To characterize the detachment forces for the thread–plaque holdfast as well as the modes of plaque failure, we use a custom-built load frame (see Fig. 2(a) for schematic, and the ESI,† for additional details) with an integrated, dual-angle imaging system. The sample is positioned below a tensile testing machine composed of a rigid clamp to which the mussel byssal thread is attached, in series with a force sensor (Honeywell Model 34 with a precision of 0.01 N and sampling rate of 1 kHz) and stepper motor, which is moved at constant rate (Haydon Series 35000). A simple microscope, consisting of an APO Macro 0.4× objective (Leica) and infinity corrected tube lens (Thor Labs ITL200), is positioned below the sample plane to enable simultaneous imaging of the debonding interface using a monochrome Firefly MV CMOS camera (Point Grey; 8-bit, 640 × 480 pixels, 60 fps). A second color camera (Hercules Classic Silver; 32-bit, 1024 × 768 pixels, 30 fps) is positioned to enable side-view imaging of the deformed plaques (Fig. 1). Each sample is illuminated at shallow angle (<20°) with an Amscope stereo illuminator (6 Watt LED). The image collection rate is adjusted, depending on the loading rate, to ensure that on the order of 500–1000 images are collected per experiment (between the initial loading and eventual debonding). To improve the accuracy of

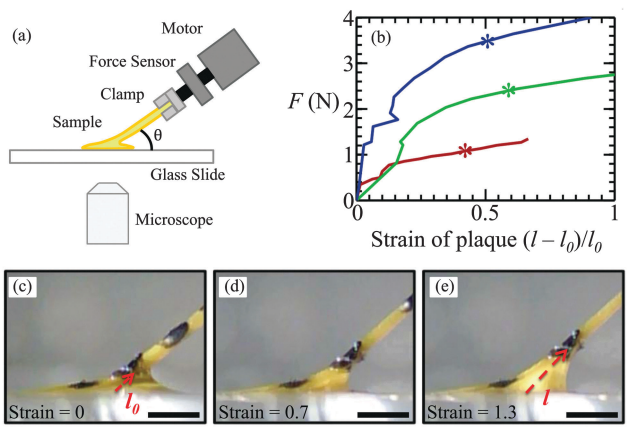

Fig. 2 (a) Schematic of experimental test frame with custom-built tensile testing system and integrated, dual-angle imaging system, which allows simultaneous measurement of force, deformation, and detachment mode. (b) Three representative examples of force verses plaque strain, measured as the distal thread is displaced at a constant rate of 30 μm s^{-1} and at an angle of 45°. For each curve, the asterisk indicates the strain at which adhesive failure initiates. (c)–(e) Side-view images of plaque deformation at three strain values; the full force *versus* strain behavior is given by the red curve in Panel (b). The scale bars are 1 mm. At the thread–plaque junction and on the edge of the plaque, black nail polish has been applied to provide trackable fiducial markers. (c) Is the first frame in the movie, where the force and strain are zero. On (c) the distance between the first nail polish mark and the glass slide is labeled l_0 by the red arrow. In subsequent frames, the distance l between the glass slide and this mark increases and the strain is defined $(l - l_0)/l_0$; the smallest resolvable strain is ~5–10% depending on l_0.

the force measurement we perform a running average at the same frequency as the images are acquired, which also syncs the image acquisition and force measurement.

The loading axis of the tensile machine is constructed onto a rotation stage that can be unlocked, rotated to a new orientation, and locked again; allowing for samples to be pulled at any angle θ, where θ is defined relative to substrate. We note that the thread typically meets the plaque at a natural angle of $\sim 5^\circ$–45°, however we do not monitor this angle during plaque formation, due to the practical difficulties of recording the motions of the mussels for several days during deposition. Rather, we measure the pulling angles with respect to the glass surface and average over several plaques at each pull angle to determine the average response. Custom-written LabVIEW software controls the stepper motor and both cameras, and allows the force, motor displacement, and both video feeds to be recorded, in addition to sample metadata (*i.e.* pull speed, pull angle, sample type, *etc.*). To ensure that the plaque and lower thread–plaque junction remain hydrated during the experiment, a small drop of water was placed on top of the plaque prior to the start of the measurement. The upper portion of the thread, near the clamped end, was not hydrated.

3 Results & discussion

3.1 Plaque strain during adhesive failure

We begin by determining the bulk deformation of the plaque during extension. In these experiments, each sample is pulled by the distal portion of the byssal thread at a constant rate of 30 μm s^{-1} and at an angle of 45°. Fig. 2(c)–(e) show representative images of a plaque undergoing deformation along the loading axis. Before the start of the experiment, black fiducial markers are painted on the outer cuticle and at the plaque–thread junction to allow measurement of plaque strain at various discrete locations on the structure. We find that as the sample is strained, the fiducial markers on the outer part of the plaque do not move within our detection level of 10 μm, but the marker at the thread–plaque junction undergoes significant displacement (strain $>100\%$). The extremely low strain near the edge is likely an intrinsic feature of the plaque geometry, since near the thread–plaque junction, the plaque thickness h_p is similar to the radial distance from the junction to the edge. Finite element models of simplified mushroom-shaped structures show that under normal loading the stress is largest underneath the thread–plaque junction and decays rapidly to zero for radial distances $>h_p$.[15] This suggests that the mussel plaque geometry may protect against adhesive failure, in a manner that is largely independent of the interfacial energy of the underlying chemical bonds.

We can also determine how strain at the thread–plaque junction correlates with force under conditions of constant thread displacement. In Fig. 2(b), we show the force–strain relationship for three representative plaques of similar size ($\sim$3.1 mm diameters). In all cases, force increases with strain, with an initial steep rise in force that turns over above a critical strain of $\sim$20%. It's not uncommon for the thread to break at forces near or larger than the forces observed at these critical strains, and in these cases, we notice that the plaques, while still adhered to the glass, are noticeably deformed and that this deformation does not seem to diminish over the time scales of minutes. Thus, it appears that above a critical strain of $\sim$20% we observe the onset of a plastic yielding regime. Through direct imaging of the debonding interface, we can also determine the strain at which the plaque debonds (indicated by an asterisk in Fig. 2(a)). In each case, we find that yielding precedes debonding. This feature may be advantageous to mussel attachment: yielding may dissipate strain energy from the applied extension, thereby reducing the energy available to separate the plaque–glass interface and increasing mussel tenacity.

Our method also allows characterization of the strain behavior of the byssal thread; however, our results are consistent with numerous prior studies of thread mechanics,[8,16,17] so are not reported here. Instead, we focus on a novel aspect of mussel holdfast mechanics: modes of failure/detachment and plaque detachment force.

3.2 Detachment

Three modes of plaque failure are observed: adhesive failure, in which a crack initiates under the thread–plaque junction and propagates radially until the plaque separates from the glass, and two modes of cohesive failure, in which the plaque itself tears apart under load.

The adhesive failure mode is illustrated in Fig. 3(f). As the distal portion of the thread is pulled at a constant rate, the force initially increases linearly with thread displacement, then begins to plateau before increasing again (Fig. 3(e)). Eventually, the force reaches a critical value and the plaque begins to separate from the glass slide. In many cases, crack initiation occurs near this maximum force, although we sometimes observe a small increase in force as the sample begins to debond. This force extension behavior is dominated by the thread mechanics since the thread is 20 mm long and the plaque is only $\sim$0.5 mm thick. The general features of the force extension plot are in agreement with those reported in prior experiments of isolated mussel byssal threads.[8,16,17]

Throughout the tensile measurement, we also image the plaque–glass interface and the bulk deformations of the plaque, as shown in Fig. 3(a)–(d). The images in panel (a) are taken at the beginning of the experiment when F = 0 N, and show the undeformed plaque shape and the plaque–glass interface when the plaque is fully adhered. The images in panel (b) are obtained when the force is maximal. Here, the plaque has been significantly deformed, and the glass-plaque interface image shows a dark area near the plaque center where the plaque has begun to lift from the glass. In all cases, adhesive failure initiates under the thread–plaque junction, rather than the plaque edge, leading to the formation of a small, roughly circular cavity. As shown in panels (c) and (d), with increased thread displacement, the cavity continues to expand radially outward until the thread–plaque completely detaches from the glass slide. This cavity expansion leads to a substantial increase in plaque strain (as shown in the

 This journal is © The Royal Society of Chemistry 2015

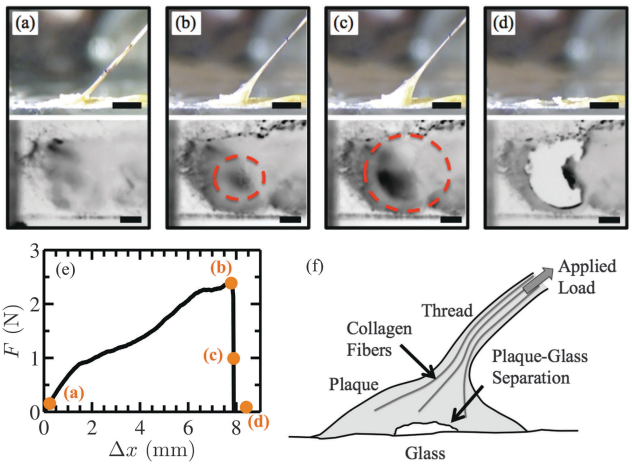

Fig. 3 Example of plaque detachment *via* adhesive failure, at pull angle 45° and pull rate 30 μm s^{-1}. (a)–(d) The top row of images shows the thread–plaque deformations from a side-view perspective, while the lower row shows the debonding interface as observed from below the glass slide (scale bars = 1 mm). The dashed red circles are drawn to be slightly larger than the crack radius and included to aid the reader in identifying the location of the propagating crack. (e) Force to extend a thread–plaque sample a distance Δ*x*. The labeled circular markers correspond to the images shown in panels (a)–(d). (f) Schematic showing the mechanism of adhesive failure in mussel plaques, where debonding is initiated at the plaque–glass interface *via* a center-initiated crack.

side-view images), but leads to little to no increase in the apparent force.

The other two modes of detachment involve cohesive failure of the plaque. In one case, plaque–plaque separation occurs within the center of the plaque under the thread–plaque junction; we call this interior cohesive failure, and an example of this mode is shown in Fig. 4. The force extension curve in Fig. 4(e) is again dominated by thread mechanics. In the lower images of panels (a)–(d) we observe that the plaque–glass

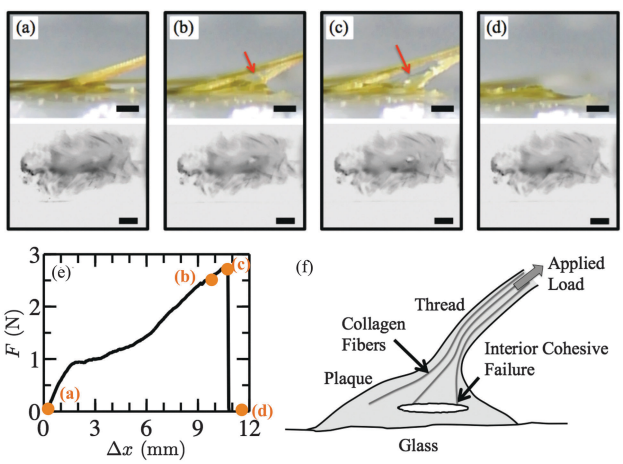

Fig. 4 Example of plaque detachment *via* interior cohesive failure, which initiates underneath the thread–plaque junction, using the same presentation style as in Fig. 3. Pull angle is 20°, and pull rate is 30 μm s^{-1}. In panels (b) and (c) the arrows indicate the location of cohesive failure. The contrast in the upper images in panels (a)–(d) has been digitally enhanced to improve visibility of the tearing plaque. Scale bars = 1 mm.

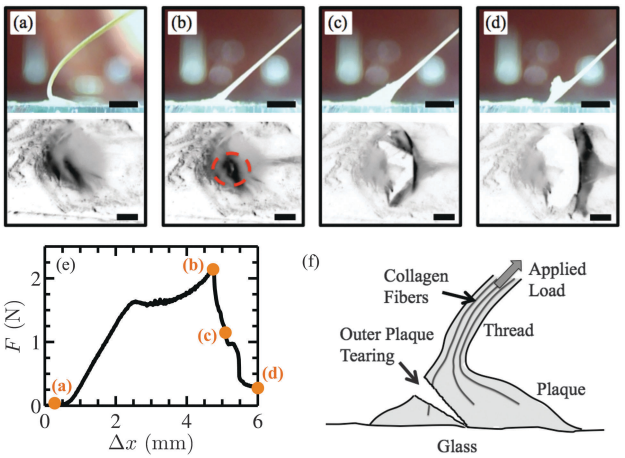

Fig. 5 Example of plaque detachment *via* exterior cohesive failure, using the same presentation style as in Fig. 3. Pull angle is 135°, and pull rate is 30 μm s^{-1}. In panel (b), the red dashed circle indicates the location of crack initiation. At these high angles, the collagen fibers at the thread–plaque junction are subjected to large bending stresses, as shown in (f). Scale bars are = 1 mm.

interface is unchanged by the extension of the thread. However, the upper images show that the plaque undergoes a significant amount of deformation as the thread is pulled, until at a critical force, the plaque begins to cohesively fail (panels (b) and (c)). In the final image, we observe that the thread–plaque junction, and upper portion of the plaque have been removed from the slide, although the plaque–glass interface is intact. This demonstrates that plaque failure does not require loss of adhesion.

The other mode of cohesive failure initiates outside the center of the plaque and a tear propagates to the glass interface; we call this exterior cohesive failure, as shown in Fig. 5. As will be described in more detail below, this mode of failure is most likely to occur at larger pull angles ($\theta > 90°$), where the sample is being folded back upon itself. At this loading angle, there appears to be a weak region on the apical side of the thread–plaque junction that allows a crack to form and propagate in a manner resembling an exterior tear. Once the plaque begins to tear apart, the crack moves downward until it reaches the glass slide, at which point the plaque peels away from the glass surface. Evidence of this detachment mode is shown in images (a)–(d). In image (b), when the force is maximal, a dark spot can be seen in the glass–plaque interface image where the crack has formed, but it is difficult to discern any evidence of cohesive failure from the side-view image. However, in images (c) and (d), it is clear that cohesive failure has occurred just outside of the thread–plaque junction and that the plaque is indeed peeling from the glass slide.

While it is possible for any of the three detachment modes to occur during a given experiment, we find that the probability of observing a particular mode depends strongly on pull angle; see Fig. 6(a), where the frequency of occurrence for each detachment mode is plotted at each pull angle. For acute pull angles ($\theta \leq 90°$), which is the more natural loading scheme, given the radial distribution of threads around the mussel body, detachment occurs only through adhesive failure or interior cohesive

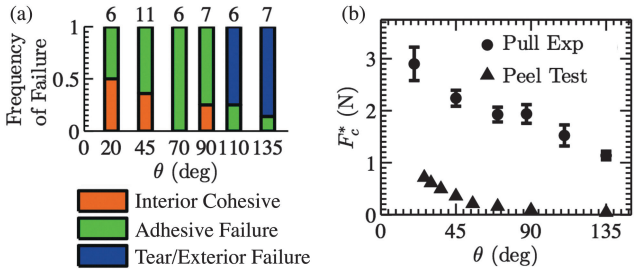

Fig. 6 Effects of pull angle on failure mode and critical force for detachment. In all cases, pull rate is fixed at 30 μm s^{-1} (a) Frequency of each failure mode as a function of pull angle. The bar color indicates type of failure mode, and the length represents the fraction of occurrences (thus total bar height at any angle = 1). The number of samples tested is placed above each bar. (b) Dependence of effective detachment force on pull angle for unaltered thread–plaque samples (circles), and peel test experiments on altered plaques, where an edge crack is initiated to induce detachment (triangles); see main text for full experimental details. Error bars represent the standard error of the mean (for peel test data, error bars are smaller than the size of the marker).

failure, and the fraction of cohesive failures increases with decreasing pull angle. This is likely due to the fact that adhesive failure is primarily governed by the loading energy along the direction normal to the glass slide. As the pull angle becomes more shallow, the force required to adhesively debond the plaque must increase to reach the critical normal loading force; however, the plaque is unable to sustain these pull forces and instead cohesively fails.[18] Recent work suggests that in-plane forces such as friction near the debonding interface may also play a role in increasing the force necessary to achieve adhesive failure at shallow pull angles.[19,20] For obtuse pull angles, $\theta \geq 90^\circ$, exterior cohesive failure dominates. The differences in cohesive failure mode at various pull angles may arise from the structural properties of the collagen fibers that run through the thread and terminate within the plaque body. At small loading angles, the majority of the fibers are loaded in tension and can therefore sustain high levels of stress. By contrast, at large angles, the fibers fail to sustain the large bending stresses, which would rarely be encountered in a natural setting, leading to the ''tear and peel'' form of cohesive failure.

To better understand the trends shown in Fig. 6(a) and how they influence mussel plaque tenacity, we also determine the average detachment force F_c, which we define as the maximum force in the force extension curve, at each pull angle. In general, the value of F_c depends upon the plaque diameter, which in our study varies between 2–6 mm. In testing 15 plaques of different sizes pulled at $\theta = 45^\circ$ and rate 30 μm s^{-1}, we observed that the detachment force scaled linearly with plaque diameter D_p (data not shown). We use this linear scaling to rescale the detachment force as follows:

$$F_c^* = F_c \times \frac{3\ \text{mm}}{D_p}, \quad (1)$$

where D_p is the measured plaque diameter and F_c* is the effective detachment force had the plaque been 3 mm in size, which is the approximate average diameter of the plaques tested.

In Fig. 6(b), we show the average of F_c* at different pull angles for samples pulled at a rate of 30 μm s^{-1}. The data show that F_c* decreases monotonically with increasing θ, varying by a factor of $\sim$3 over the range of angles tested (20–135°). In all cases, the force to initiate mechanical adhesive failure increases with decreasing pull angle, and at the largest and smallest angles, the plaque is more likely to cohesively fail than to lose adhesion. Mussels typically hold the byssal threads in tension at angles of 5–45°. Although we find a modest dependence of pulling angle on the critical force for detachment overall, we do find the largest debonding forces in this regime, in which both adhesive failure and interior cohesive failure occur. High-angle pulls are unlikely to occur in a natural setting, due to the radial distribution of byssal threads around the mussel body, and the lack of evolutionary pressure may explain why this is the weakest of the failure modes.

3.3 Fracture energy

To better understand how strain energy is released during plaque debonding, we determine the plaque–glass fracture energy, defined as the energy dissipated per unit of new surface area created by the separation of two dissimilar materials. Experimentally, we employ a peel test,[18] in which we record the force required to peel a strip of plaque from a glass slide at fixed pull angle and speed. To carry out a peel test on a plaque adhered to glass, it would be ideal if the geometry consisted of a strip of plaque of uniform width, with an initiated crack, that is being peeled from the glass surface. Since we cannot force the mussel to produce plaques with such a geometry, we instead modify the plaque to mimic a strip geometry to the best of our ability. To do this, we acquire plaques attached to glass slides as previously described. We then use a clean razor blade to slice straight through the plaque on either side of the thread. The outer portions of these cuts are removed and discarded. The two cuts are made $\sim$1 mm apart and are parallel to the direction the thread joins the plaque and to each other. Once the outer portions are removed, the razor is lightly pressed into the perpendicular edge under the thread–plaque junction and at the plaque–glass interface to initiate a crack. This results in a strip of near uniform width that can be pulled *via* the thread. As before, the motor is clamped to the thread $\sim$20 mm from the plaque. In Fig. 7(b) an image of prepared strip of plaque is shown. For each peel test we pull on the thread at angle θ and rate 30 μm s^{-1} while recording the pull force F. In Fig. 7, we show a representative result, in which a plaque is pulled at $\theta = 25^\circ$. Fig. 7(a) shows the force during the peel test as the motor displaces the distal thread of the sample a distance Δx. During the test, there is an initial increase in force as the sample is slightly strained, and eventually the force reaches a plateau value which is the critical force to propagate the crack. Images of the crack propagation are shown in Fig. 7(c)–(e) and the moving crack fronts are marked by the red arrows.

Using a simple model of peeling mechanics, we can extract the fracture energy, the energy dissipated during fracture per unit of newly created surface area. Experimentally, we repeat these measurements at angles varying from 25–135°, and the

 This journal is © The Royal Society of Chemistry 2015

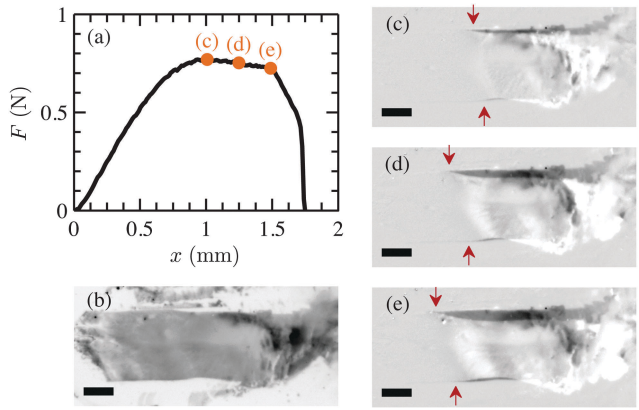

Fig. 7 Representative data and images from a peel test for a plaque pulled at an angle of 25°. (a) Force extension curve as the thread is pulled and the plaque peels. The circular markers correspond to the sequential snapshots of the peeling plaque in panels (c)–(e). (b) Raw image of plaque at the beginning of the experiment. (c)–(e) Difference images, obtained through subtraction of an image at a desired time point and the initial image shown in panel (b). These difference images highlight changes that occurred since the beginning of the experiment and in particular allow the propagating crack front as the plaque debonds from the glass slide to be observed. The red arrows point to the edge of the moving crack which travels from right to left in this time sequence. Scale bars are 500 μm.

results are shown in Fig. 8. We fit these data to theoretical predictions for peel strength F_c/b, assuming that the strip can be well-approximated by Kendall's treatment of a thin, inextensible film:

$$F_c/b = G_c/(1 - \cos(\theta)), \quad (2)$$

where G_c is the fracture energy.[18] For large angles (and thus small values of $1/(1 - \cos(\theta))$), the data show the anticipated linear trend, and by fitting the slope of the line in this regime, we obtain a fracture energy of 96 ± 6 J m^{-2}, which is comparable to the measured values of other flexible, adhesive laminates and tapes.[21–23]

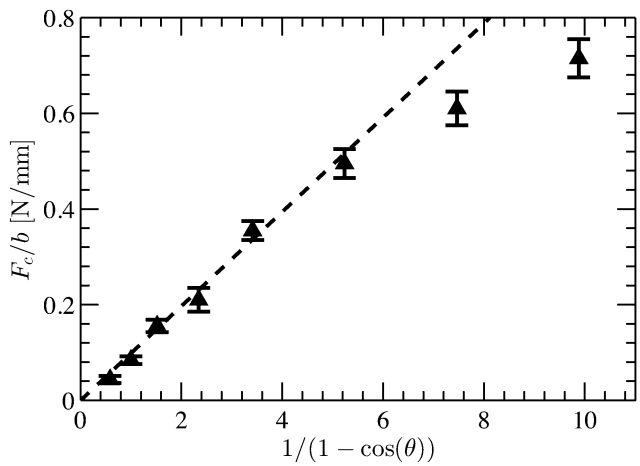

Fig. 8 Average force per unit crack length to peel a plaque at an angle θ and rate 30 μm s^{-1}. Each data point is the average of two trials, and the error bars are the algebraic sum of the standard deviation of the data and the measurement error of the force sensor (±0.02 N). The black dashed line is a non-weighted linear fit using eqn (2) for $\theta \geq 37°$. The fit gave a fracture energy G_c = 96 ± 6 J m^{-2}.

In this form of Kendall's model, it is assumed that the elastic energy of the film and substrate can be ignored. Note that at larger angles (small $1 - \cos(\theta)$) the force to peel the plaque is more than 10 times smaller than the force to debond an unaltered plaque; see Fig. 6b. At these forces, the thread and plaque deform little and the approximation to ignore the elastic energy is reasonable. This is further confirmed by the linearity of the plot for $\theta \leq 40°$. For small angles (and thus larger values of $1/(1 - \cos(\theta))$) the elastic and dissipative properties of the material begin to play more important roles in determining the force to debond, and we find that the model systematically overestimates the peel strength, in agreement with prior studies of adhesive films.[24,25] Although models exist to account for such deviations,[19,20,26] we do not yet have a complete understanding of the bulk elastic and dissipative processes of the holdfast, and do not attempt to add these contributions into the model presented here.

Our determination of plaque fracture energy now allows comparisons with prior reports of the energies required to separate mica surfaces coated with various mussel foot proteins found in the plaque using the surface force apparatus (SFA).[1] The mussel foot proteins are naturally enriched in 3,4-dihydroxy-L-phenylalanine (DOPA), a functionality that plays an important role in underwater adhesion.[27] In such SFA experiments, the surfaces are slowly moved to maintain equilibrium, and therefore the measured interfacial energies are dominated by the molecular-level breakage of the adhesive bonds. The observed interfacial energies for mfp-1, mfp-3, and mfp-5 are typically ~(0.1–10) × 10^{-3} J m^{-2}, which is 4–6 orders of magnitude smaller than the fracture energies we determined for intact mussel plaques.[28,29] This large discrepancy indicates the importance of supramolecular-level dissipative mechanisms within the mussel holdfast that substantially enhance its tenacity. The structural origins of these additional dissipative mechanisms are not yet known and will be the focus of further studies.

The peel test results also provide a unique opportunity to determine the role of holdfast shape on the detachment force. By comparing the peel test results to our previous measurements on the forces to detach natural mussel plaques, we can assess the importance of the location of crack initiation on tenacity. As shown in Fig. 6, we find the natural plaque shape improves the bond strength by nearly an order of magnitude. In the peel test, we initiate an edge crack using a razor blade, which effectively places the thread at the edge of the plaque, mimicking a spatula geometry rather than the mushroom-shaped geometry of the natural mussel holdfast. In nature, both the spatula and mushroom-shaped geometries are commonly employed by other organisms. The spatula geometry is typically employed by organisms that require transient attachment (*i.e.* flies or beetles that temporarily land before continuing flight), while organisms employing a mushroom-shaped holdfast require strong long term bonds (*i.e.* mussels, creeping vines, *etc.*).[11]

Additionally, we find that relative change in critical force over the range of angles measured by the peel test is ~2 times higher than those measured in the pull geometry. This suggests that the spatula shape gives slightly greater tunability in detachment force when pull angle is varied, albeit at the expense of a

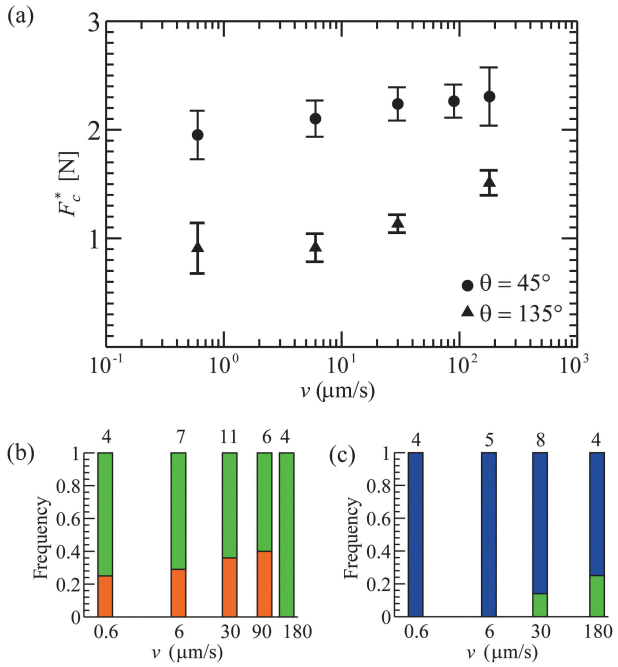

Fig. 9 (a) Effect of pull rate on the critical detachment force. Error bars represent the standard error of the mean. (b and c) Are the pull rate dependent probabilities to observe a particular detachment mode at pull angles 45° and 135° respectively. The bar graphs follow the same format as in Fig. 6.

weaker overall adhesive strength. Our results highlight important considerations for designing adhesive holdfasts: by controlling the placement of the thread–plaque junction, it is possible to vary the adhesive strength as well as the extent to which that strength can be tuned *in situ* by adjusting the direction of applied load.

3.4 Rate dependence

Finally, we explore the role of pull rate on the dynamics of the detachment by determining its effect on the failure mode and detachment force by pulling samples at angles $\theta = 45^\circ$ or 135° at constant pull rates v between 0.6 μm s^{-1} to 180 μm s^{-1}. In contrast to the strong effects we observed by varying pull angle, we find no dependence of failure mode and a weak dependence in pull force with v (Fig. 9). When the pull rate was varied by over two orders of magnitude, the detachment force only changed by ∼20% for $\theta = 45^\circ$ where adhesive failure dominates, and by ∼50% for pull angle $\theta = 135^\circ$ where exterior cohesive failure primarily occurs. In nature, pull angles of ∼45° are more common, and the insensitivity of attachment strength on pull rate in this regime may protect mussels against a wide range of wave speeds, as well as predatory attacks that could exploit a specific rate-dependence to dislodge and capture mussels.

4 Conclusion

By studying the detachment dynamics of adhered mussel plaques under applied loads, we investigated how various aspects of the contact mechanics, such as shape, bulk deformation, pull direction, pull rate, and fracture energy contribute to both the attachment strength and mode of failure of *Mytilus californianus* plaques. Similar mushroom-shaped adhesive structures are commonly employed by organisms to maintain strong longterm bonds, suggesting that this contact geometry is particularly effective for strong adhesion.[11] Here we find that the detachment dynamics of these structures are quite rich, and that the details of the plaque shape and mechanics, as well as the loading scheme, are all important in determining the attachment strength and mode of failure. These results provide new insight into optimization of adhesive structure design.

A key feature to enhancing adhesion is the ability to direct and dissipate the strain energy applied to the structure to suppress debonding. Our experiments show that the mussel's holdfast is quite deformable, with a plastic yield point at ∼20% strain. Dissipation of energy through plasticity may reduce the energy available to adhesively separate the plaque–glass interface, resulting in a stronger adhesive bond. Many dissipative plastic processes are rate dependent, particularly in biological materials where molecular bond breakage and protein unfolding often play important roles. However, we found the adhesive strength of the plaque to only have a slight dependence on pull speed. Although the microscopic origins of this rate-independence are not yet understood, there is a clear evolutionary advantage, since waves and predators will undoubtedly apply loads at a variety of rates that mussels must withstand.

We also found relatively small contributions to the fracture energy from the molecular bonds at the plaque–glass interface. Although many point to the impressive chemical bond strength of the catechol moieties present in the plaque as the primary reason that mussels can form strong permanent bonds to substrates, our results demonstrate that a large component of the adhesive strength arises from control of dissipative processes within the mussel holdfast. Similar phenomena were recently observed in cobweb-weaving spiders, which exploit changes in the architecture of their attachment disks, rather than in the chemistry of the silk that forms the thread to achieve different functions, such as locomotion or prey capture.[30,31] Thus, geometric and mechanical control may be a general feature of biological adhesives. This also suggests new avenues for bio-inspired material design, that go beyond simple manipulation of the composition and strength of the chemical bonds at the interface to include mechanically complex adhesive structures to control and direct strain energy throughout the material.[31]

Acknowledgements

This work was supported by the MRSEC Program of the National Science Foundation (NSF) under Award DMR 1121053, a Burroughs Wellcome Career Award at the Scientific Interface (to MTV) and the Natural Sciences and Engineering Research Council (NSERC) of Canada (post-graduate scholarship to NAZ). Authors thank Emmanouela Filippidi, Rachel Colino, Jacob Israelachvili, Robert McMeeking and Matthew

 This journal is © The Royal Society of Chemistry 2015

Begley for helpful discussions, and Nadine Martinez Rodriguez for assistance with mussel mariculture.

References

1 B. P. Lee, P. B. Messersmith, J. N. Israelachvili and J. H. Waite, *Annu. Rev. Mater. Res.*, 2011, **41**, 99–132.
2 J. D. Witman and T. H. Suchanek, *Mar. Ecol.: Prog. Ser.*, 1984, **16**, 259–268.
3 K. Nagaya, Y. Matsui, H. Ohira, A. Yuasa, H. Yamamoto, K. Ohkawa and Y. Magara, *Biofouling*, 2001, **17**, 263–274.
4 D. J. Crisp, G. Walker, G. A. Young and A. B. Yule, *J. Colloid Interface Sci.*, 1985, **104**, 40–50.
5 H. G. Silverman and F. F. Roberto, *Mar. Biotechnol.*, 2007, **9**, 661–681.
6 E. Carrington, *Integr. Comp. Biol.*, 2002, **42**, 846–852.
7 J. H. Waite, N. H. Andersen, S. Jewhurst and C. Sun, *J. Adhes.*, 2005, **81**, 297–317.
8 E. Bell and J. Gosline, *J. Exp. Biol.*, 1996, **199**, 1005–1017.
9 R. Spolenak, S. Gorb, H. Gao and E. Arzt, *Proc. – R. Soc. Edinburgh, Sect. A: Math.*, 2005, **461**, 305–319.
10 G. Carbone, E. Pierro and S. N. Gorb, *Soft Matter*, 2011, **7**, 5545–5552.
11 S. N. Gorb and M. Varenberg, *J. Adhes. Sci. Technol.*, 2007, **21**, 1175–1183.
12 S. Gorb, M. Varenberg, A. Peressadko and J. Tuma, *J. R. Soc., Interface*, 2007, **4**, 271–275.
13 Z. Qin and M. J. Buehler, *Nat. Commun.*, 2013, **4**, 2187.
14 J. R. Burkett, J. L. Wojtas, J. L. Cloud and J. J. Wilker, *J. Adhes.*, 2009, **85**, 601–615.
15 A. V. Spuskanyuk, R. M. McMeeking, V. S. Deshpande and E. Arzt, *Acta Biomater.*, 2008, **4**, 1669–1676.
16 J. E. Smeathers and J. F. V. Vincent, *J. Mollus. Stud.*, 1979, **45**, 219–230.
17 H. A. Price, *J. Zool.*, 1981, **194**, 245–255.
18 K. Kendall, *J. Phys. D: Appl. Phys.*, 1971, **4**, 1186.
19 M. R. Begley, R. R. Collino, J. N. Israelachvili and R. M. McMeeking, *J. Mech. Phys. Solids*, 2013, **61**, 1265–1279.
20 P. Gialamas, B. Völker, R. R. Collino, M. R. Begley and R. M. McMeeking, *Int. J. Solids Struct.*, 2014, **51**, 3003–3011.
21 A. Gent and S. Kaang, *J. Appl. Polym. Sci.*, 1986, **32**, 4689–4700.
22 A. Kinloch, C. Lau and J. Williams, *Int. J. Fract.*, 1994, **66**, 45–70.
23 B. Z. Newby and M. K. Chaudhury, *Langmuir*, 1998, **14**, 4865–4872.
24 N. Amouroux, J. Petit and L. Léger, *Langmuir*, 2001, **17**, 6510–6517.
25 J. Y. Chung and M. K. Chaudhury, *J. Adhes.*, 2005, **81**, 1119–1145.
26 B. Z. Newby and M. K. Chaudhury, *Langmuir*, 1997, **13**, 1805–1809.
27 H. Lee, N. F. Scherer and P. B. Messersmith, *Proc. Natl. Acad. Sci. U. S. A.*, 2006, **103**, 12999–13003.
28 Q. Lin, D. Gourdon, C. Sun, N. Holten-Andersen, T. H. Anderson, J. H. Waite and J. N. Israelachvili, *Proc. Natl. Acad. Sci. U. S. A.*, 2007, **104**, 3782–3786.
29 E. W. Danner, Y. Kan, M. U. Hammer, J. N. Israelachvili and J. H. Waite, *Biochemistry*, 2012, **51**, 6511–6518.
30 V. Sahni, J. Harris, T. A. Blackledge and A. Dhinojwala, *Nat. Commun.*, 2012, **3**, 1106.
31 D. Jain, V. Sahni and A. Dhinojwala, *J. Polym. Sci., Part B: Polym. Phys.*, 2014, **52**, 553–560.